ARGONNE NATIONAL LABORATORY
9700 South Cass Avenue
Argonne, Illinois 60439

ANL/MCS-TM-247

Numerical Simulations of Magnetic Reversal in Layered Spring Magnets*

by

J. Samuel Jiang,† *Hans G. Kaper,*‡ *and Gary K. Leaf* §

Mathematics and Computer Science Division

Technical Memorandum ANL/MCS-TM-247

January 2001

*This work was supported by the Mathematical, Information, and Computational Sciences Division subprogram of the Office of Advanced Scientific Computing, U.S. Department of Energy, under Contract W-31-109-Eng-38.

†Materials Science Division, Argonne National Laboratory, Argonne, IL 60439 (jiang@anl.gov)

‡Mathematics and Computer Science Division, Argonne National Laboratory, Argonne, IL 60439 (kaper@mcs.anl.gov)

§Mathematics and Computer Science Division, Argonne National Laboratory, Argonne, IL 60439 (leaf@mcs.anl.gov)

Contents

Numerical Simulations of Magnetic Reversal in Layered Spring Magnets

by

J. Samuel Jiang, Hans G. Kaper, and Gary K. Leaf

Abstract. This report summarizes the results of numerical investigations of magnetic reversal in layered spring magnets. A one-dimensional model is used of a film consisting of several atomic layers of soft material on top of several atomic layers of hard material. Each atomic layer is taken to be uniformly magnetized, and spatial inhomogeneities within an atomic layer are neglected. The state of such a system is described by a chain of magnetic spin vectors. Each spin vector behaves like a spinning top driven locally by the effective magnetic field and subject to damping (Landau–Lifshitz–Gilbert equation). A numerical integration scheme for the LLG equation is presented that is unconditionally stable and preserves the magnitude of the magnetization vector at all times. The results of numerical investigations for a bilayer in a rotating in-plane magnetic field show hysteresis with a basic period of 2π at moderate fields and hysteresis with a basic period of π (or any multiple thereof) at strong fields.

1 Introduction

Exchange-spring coupled magnets (*spring magnets*, for short) hold significant promise for applications in information recording and storage devices. Spring magnets consist of nano-dispersed hard and soft magnetic phases that are coupled at the interfaces. (In a hard material, the magnetic moment tends to be aligned with the easy axis; in a soft material, it is more or less free to align itself with the local magnetic field.) The superior magnetic properties of a spring magnet stem from the fact that the soft phase enhances the magnetization of the composite [1, 2, 3, 4, 5, 6]. Since the performance of a spring magnet is determined by the stability of the soft phase against magnetization reversal, it is important to identify the factors affecting the reversal process.

Thin films provide an interesting class of simple models for which one can perform both physical and computational experiments. A spring-magnet structure can be realized by interleaving hard and soft magnetic layers, and because the layered structure results in variations of the magnetic properties predominantly along the normal direction, the structure of such spring magnets is essentially one dimensional.

In this report we investigate magnetic reversal in a hard/soft bilayer—a layer of soft material on top of a layer of hard material—with strong coupling at the interface. The hard and soft layers both consist of several atomic layers; each atomic layer is treated as

uniformly magnetized, and spatial inhomogeneities within an atomic layer are neglected. The state of the bilayer is thus described by a chain of spins in the normal direction, where each spin represents the magnetic moment of an atomic layer.

The dynamics of a magnetic moment are entirely local. A magnetic moment is like a spinning top, which is driven by the effective magnetic field and subject to damping. The relevant equation was first formulated by Landau and Lifshitz [7] and later given in an equivalent form by Gilbert [8]. The local effective field is derived variationally from an energy functional [9].

A hard material is characterized by a large anisotropy energy, which enhances the tendency of the spins to line up with the easy axis. In the soft material, on the other hand, the spins are more or less free to align themselves with the magnetic field. If the direction of the applied field deviates from the easy axis of the hard material, and the hard and soft layers are tightly coupled at the interface as in a spring magnet, the chain of spins will twist through the soft material to approach the direction of the applied field. The direction of this twist (the *chirality*) depends on the angle between the direction of the applied field and the easy axis of the hard material. It can be positive (the in-plane angle of the spin with the easy axis increases as one goes from the hard to the soft layers) or negative (the in-plane angle of the spin with the easy axis decreases as one goes from the hard to the soft layers). Transitions from one chirality to the other may occur at critical directions of the applied field. A change of chirality leads to hysteresis.

In this report we investigate magnetic reversal in a hard/soft bilayer induced by the rotation of an in-plane magnetic field. The results of numerical simulations for a Sm-Co/Fe bilayer show different behavior depending on the strength of the applied field.

- As long as the field is weak, the magnetization is reversible, and no hysteresis occurs.
- A sufficiently strong field pulls the magnetic spins in the soft layers in its wake but leaves the spins in (most of) the hard layers fixed along the easy axis. When the direction of the applied field deviates significantly from the easy direction, a transition occurs in the soft layers that changes the chirality of the chain of spins. Rotational hysteresis with a basic period of 360 degrees results. The degree of hysteresis varies with the field strength, and there is the possibility of a discontinuity because of a structural change in the chain of spins. This structural change shows some characteristics of a phase transition.
- A very strong field pulls the entire chain of magnetic spins, in the soft as well as the hard layers, in its wake. But since the spins in the hard layers are essentially confined to the easy axis, either in the positive or in the negative direction, the spins in the hard layers follow intermittently, flipping only when the direction of the applied field deviates sufficiently from the easy direction. The spins in the soft layers follow the direction of the applied field more closely as one goes up through the soft layers, but

still discontinously when the spins in the hard layers flip their orientation. Only the spin in the top layer rotates continuously. The chirality of the chain of spins does not change; however, since the chain of spins behaves more like a spring than a stiff rod, it still experiences rotational hysteresis. The period of this hysteresis can be any multiple of 180 degrees.

The numerical results explain the experimental observation of hysteresis in some torque measurements [10]. They also agree qualitatively with some magneto-optical measurements of the magnetization angle [11]. However, they differ at the quantitative level; in particular, the width of the hysteresis loops is found to be significantly greater in the simulations than in the experiments, except at weak fields. The discrepancy is due to the mathematical model: A one-dimensional model is a single-domain model, which does not allow for the nucleation and motion of nanodomains. Hence, the demagnetization energy is seriously overestimated. In simulations of realistic spring magnets, it is therefore necessary to use multidimensional models. A summary of the data presented in the present report is given in [12].

Following is an outline of the report. In Section 2 we describe the computational model and the approximation procedure. In Section 3, we present the results of the numerical simulations. In Section 4, we summarize our conclusions. We use the Gaussian C.G.S. system of units.

2 Computational Model

A layered spring magnet is a multilayer structure, which consists of N_h atomic layers of a hard magnetic material adjacent to N_s atomic layers of a soft magnetic material,

$$\begin{aligned} \text{Hard layers}: &\quad i \in I_h = \{1, \ldots, N_h\}, \\ \text{Soft layers}: &\quad i \in I_s = \{N_h + 1, \ldots, N_h + N_s\}. \end{aligned}$$

We put $I = I_h \cup I_s$ and $N = N_h + N_s$. The atomic layers are homogeneous, and variations occur only in the direction normal to the layers. We assume for convenience that the atomic layers are equally thick; their thickness d is of the order of angstroms (1 Å equals $1 \cdot 10^{-8}$ cm).

We adopt a right-handed Cartesian (x, y, z) coordinate system, where the x and y axes are in the plane of an atomic layer, the x axis coincides with the easy axis of the hard material, and the z axis is in the direction normal to the layers; $\boldsymbol{e}_x$, $\boldsymbol{e}_y$, and $\boldsymbol{e}_z$ are the unit vectors in the direction of increasing x, y, and z, respectively. In a polar (ϕ, θ) coordinate system, ϕ is the out-of-plane angle and θ the in-plane angle measured counterclockwise from the positive x axis.

The state of the bilayer is completely described by the set of *magnetic moments*,

$$\boldsymbol{M} = \{\boldsymbol{M}_i : i \in I\}. \tag{2.1}$$

Each $\boldsymbol{M}_i$ is a vector-valued function of time t, with components $M_{i,x}$, $M_{i,y}$, and $M_{i,z}$. The magnitude M_i of $\boldsymbol{M}_i$ is the *magnetization* (emu/cm^3), the unit vector $\boldsymbol{m}_i = \boldsymbol{M}_i/M_i$ is the *magnetic spin* in the ith layer. The magnetization is constant at all times and equal to the local saturation magnetization,

$$\boldsymbol{M}_i(t) = M_i \boldsymbol{m}_i(t), \quad \text{with } M_i = \begin{cases} M_h & \text{if } i \in I_h, \\ M_s & \text{if } i \in I_s. \end{cases} \tag{2.2}$$

Here, M_h and M_s are the values of the saturation magnetization for the hard and soft material, respectively. Each magnetic spin can be specified in terms of its Cartesian or polar components,

$$\boldsymbol{m}_i = (m_{i,x}, m_{i,y}, m_{i,z})^{\mathrm{t}} = (\cos\phi_i \cos\theta_i, \cos\phi_i \sin\theta_i, \sin\phi_i)^{\mathrm{t}}. \tag{2.3}$$

Thus, θ_i is the *in-plane* angle of $\boldsymbol{m}_i$ with the easy axis of the hard material (measured from the positive x direction), ϕ_i the *out-of-plane* angle of $\boldsymbol{m}_i$.

2.1 Dynamics of the Magnetic Moment

In the one-dimensional model under consideration, the dynamics of the magnetic moment are entirely local and are those of a spinning top subject to damping. The force driving $\boldsymbol{M}_i$ is the local magnetic field $\boldsymbol{H}_i$. The equation of motion is the Landau–Lifshitz–Gilbert (LLG) equation,

$$\frac{\partial \boldsymbol{M}_i}{\partial t} = -\gamma(\boldsymbol{M}_i \times \boldsymbol{H}_i) + \frac{g}{M_i}\left(\boldsymbol{M}_i \times \frac{\partial \boldsymbol{M}_i}{\partial t}\right), \quad i \in I. \tag{2.4}$$

Here, γ is the gyromagnetic constant (sec^{-1}oersted^{-1}) and g a (dimensionless) damping coefficient. The magnitude of $\boldsymbol{H}_i$ is specified in oersted (1 oersted = 1 emu/cm^3). Note that the LLG equation yields a magnetic moment whose magnitude is constant in time. An equivalent form of the LLG equation is

$$\frac{\partial \boldsymbol{M}_i}{\partial t} = -c\left[(\boldsymbol{M}_i \times \boldsymbol{H}_i) + \frac{g}{M_i}\boldsymbol{M}_i \times (\boldsymbol{M}_i \times \boldsymbol{H}_i)\right], \quad i \in I, \tag{2.5}$$

where $c = \gamma/(1+g^2)$.

Suppose that the system is subject to an externally applied magnetic field $\boldsymbol{H}_a$, which is uniform and constant in time. Then the local magnetic field $\boldsymbol{H}_i$ is computed at any time from the expression

$$\begin{aligned} \boldsymbol{H}_i = \boldsymbol{H}_a \; &+ \; \frac{1}{M_i}\left[J_{i,i+1}(\boldsymbol{m}_{i+1} - \boldsymbol{m}_i) - J_{i,i-1}(\boldsymbol{m}_i - \boldsymbol{m}_{i-1})\right] - 2\frac{K_i}{M_i}\boldsymbol{e}_x \times (\boldsymbol{m}_i \times \boldsymbol{e}_x) \\ &- \; 4\pi M_i(\boldsymbol{m}_i \cdot \boldsymbol{e}_z)\boldsymbol{e}_z, \quad i \in I, \end{aligned} \tag{2.6}$$

where

$$\boldsymbol{m}_0 = \boldsymbol{m}_1, \ \boldsymbol{m}_{N+1} = \boldsymbol{m}_N. \tag{2.7}$$

The last identities are the discrete analogs of the Neumann boundary condition at the free surfaces (no surface anisotropy); $\boldsymbol{m}_0$ and $\boldsymbol{m}_{N+1}$ may be viewed as the magnetic spins in a virtual layer of hard material at the bottom (index $i = 0$) and a virtual layer of soft material at the top (index $i = N + 1$).

The coupling coefficient J (erg/cm^3) has the same value between layers of the same material; similarly, the anisotropy coefficient K (erg/cm^3) is constant within the same material,

$$J_{i,i+1} = \begin{cases} J_h, & i = 1, \ldots, N_h - 1, \\ J_{hs}, & i = N_h, \\ J_s, & i = N_h + 1, \ldots, N, \end{cases} \qquad K_i = \begin{cases} K_h, & i = 1, \ldots, N_h, \\ K_s, & i = N_h + 1, \ldots, N. \end{cases} \tag{2.8}$$

The actual values of these material parameters depend on the temperature; $K_s \ll K_h$ in all practical cases.

The expression (2.6) is an approximation for the expression

$$\boldsymbol{H}_i = \boldsymbol{H}_a - \frac{\delta F}{\delta \boldsymbol{M}_i}, \tag{2.9}$$

where F is the free energy density and $\delta/\delta \boldsymbol{M}_i$ its Fréchet derivative with respect to $\boldsymbol{M}_i$. The free energy is the sum of the exchange energy, the anisotropy energy, and the demagnetization energy,

$$\mathcal{F}[\boldsymbol{M}] = \int_\Omega \left[\frac{1}{2} A(z) \left| \frac{\partial \boldsymbol{m}}{\partial z} \right|^2 + K(z) \, |\boldsymbol{m} \times \boldsymbol{e}_x|^2 + \frac{1}{2} (4\pi) (\boldsymbol{M} \cdot \boldsymbol{e}_z)^2 \right]. \tag{2.10}$$

Here, Ω is the z interval occupied by the entire multilayered structure and A is the exchange coupling coefficient (erg/cm), which is related to J ($J = Ad^{-2}$). The demagnetization tensor for a layer has only one element, D_{zz}; 4π is its value for an infinitely thin flat ellipsoid [13]. Note that 1 emu equals 1 erg/oersted and 1 oersted equals 1 emu/cm^3, so F is expressed in units of erg/cm^3.

2.2 Integration of the LLG Equation

The LLG equation maintains a constant magnetization, so the only quantity that changes in the course of time is the direction of the magnetic moment. We therefore begin by rewriting the LLG equation in terms of $\boldsymbol{m}$. As the equation is entirely local to each layer, we drop the index i temporarily. We use the prime $'$ to denote differentiation with respect to time.

Let H be the strength of the magnetic field (oersted), and let $\boldsymbol{h} = \boldsymbol{H}/H$ be the unit vector in the direction of $\boldsymbol{H}$,

$$\boldsymbol{H}(t) = H(t)\boldsymbol{h}(t). \tag{2.11}$$

Then the LLG equation is

$$\boldsymbol{m}' = -cH\left[(\boldsymbol{m}\times\boldsymbol{h}) + g\boldsymbol{m}\times(\boldsymbol{m}\times\boldsymbol{h})\right]. \tag{2.12}$$

We decompose the equation by means of the projection operators P and Q,

$$P\boldsymbol{u} = (\boldsymbol{u}\cdot\boldsymbol{h})\boldsymbol{h},\ Q\boldsymbol{u} = \boldsymbol{u} - P\boldsymbol{u} = \boldsymbol{h}\times(\boldsymbol{u}\times\boldsymbol{h}), \quad \boldsymbol{u}\in\mathbf{R}^3. \tag{2.13}$$

Equation (2.12) is equivalent to the two equations

$$P\boldsymbol{m}' = -cHP\left[(\boldsymbol{m}\times\boldsymbol{h}) + g\boldsymbol{m}\times(\boldsymbol{m}\times\boldsymbol{h})\right], \tag{2.14}$$

$$Q\boldsymbol{m}' = -cHQ\left[(\boldsymbol{m}\times\boldsymbol{h}) + g\boldsymbol{m}\times(\boldsymbol{m}\times\boldsymbol{h})\right]. \tag{2.15}$$

Notice the identities

$$P(\boldsymbol{m}\times\boldsymbol{h}) = \mathbf{0},\ P[\boldsymbol{m}\times(\boldsymbol{m}\times\boldsymbol{h})] = (\boldsymbol{m}\cdot Q\boldsymbol{m})\boldsymbol{h} = -[1-(P\boldsymbol{m}\cdot P\boldsymbol{m})^2]\boldsymbol{h}, \tag{2.16}$$

$$Q(\boldsymbol{m}\times\boldsymbol{h}) = -JQ\boldsymbol{m},\ Q[\boldsymbol{m}\times(\boldsymbol{m}\times\boldsymbol{h})] = (\boldsymbol{m}\cdot\boldsymbol{h})Q\boldsymbol{m}, \tag{2.17}$$

where J is the square root of the negative identity in $\mathbf{R}^2$,

$$I = \begin{pmatrix} 1 & 0 \\ 0 & 1 \end{pmatrix},\ J = \begin{pmatrix} 0 & -1 \\ 1 & 0 \end{pmatrix},\ J^2 = -I. \tag{2.18}$$

Hence, we can recast Eqs. (2.14) and (2.15) in the form

$$P\boldsymbol{m}' = cgH[1-(P\boldsymbol{m}\cdot P\boldsymbol{m})^2]\boldsymbol{h}, \tag{2.19}$$

$$Q\boldsymbol{m}' = cH[J - g(\boldsymbol{m}\cdot\boldsymbol{h})I]Q\boldsymbol{m}. \tag{2.20}$$

Suppose that the direction of $\boldsymbol{H}$ does not change on an interval $(t, t+\Delta t)$,

$$\boldsymbol{h}(s) = \boldsymbol{h}(t), \quad s\in(t,t+\Delta t). \tag{2.21}$$

Then $P\boldsymbol{m}' = (P\boldsymbol{m})'$ and $Q\boldsymbol{m}' = (Q\boldsymbol{m})'$ on $(t,t+\Delta t)$, so Eqs. (2.19) and (2.20) reduce to a coupled system of differential equations for the scalar $u = (P\boldsymbol{m}\cdot\boldsymbol{h})$ in $\mathbf{R}$ and the vector $\boldsymbol{v} = Q\boldsymbol{m}$ in $\mathbf{R}^2$,

$$u' = cgH(1-u^2) \quad \text{on } (t,t+\Delta t). \tag{2.22}$$

$$\boldsymbol{v}' = cH(J-guI)\boldsymbol{v} \quad \text{on } (t,t+\Delta t). \tag{2.23}$$

From these equations we conclude that the critical states are $u=1$, $\boldsymbol{v}=\mathbf{0}$ ($\boldsymbol{m}=\boldsymbol{h}$, magnetic moment parallel to the magnetic field) and $u=-1$, $\boldsymbol{v}=\mathbf{0}$ ($\boldsymbol{m}=-\boldsymbol{h}$, magnetic

moment antiparallel to the magnetic field). The former is linearly stable, the latter unstable under infinitesimal perturbations.

We now turn to the integration of Eqs. (2.22) and (2.23). The former is independent of $\boldsymbol{v}$ and can be integrated immediately. If not only the direction but also the magnitude of H is constant on $(t, t+\Delta t)$,

$$\boldsymbol{H}(s) = \boldsymbol{H}(t), \quad s \in (t, t+\Delta t), \tag{2.24}$$

we find

$$u(s) = \frac{u(t)\cosh(cgH(t)(s-t)) + \sinh(cgH(t)(s-t))}{\cosh(cgH(t)(s-t)) + u(t)\sinh(cgH(t)(s-t))}, \quad s \in (t, t+\Delta t). \tag{2.25}$$

Next, we turn to Eq. (2.23). We replace the constant cgH by $u'/(1-u^2)$ (from Eq. (2.22)) and use the identity $-uu'/(1-u^2) = (\ln(1-u^2)^{1/2})'$ to convert the equation into a differential equation for the vector $\boldsymbol{w} = (1-u^2)^{-1/2}\boldsymbol{v}$,

$$\boldsymbol{w}' = cHJ\boldsymbol{w} \quad \text{on } (t, t+\Delta t). \tag{2.26}$$

This equation can be integrated,

$$\begin{aligned} \boldsymbol{w}(s) &= \mathrm{e}^{cH(t)(s-t)J}\boldsymbol{w}(t) \\ &= [\cos(cH(t)(s-t))I + \sin(cH(t)(s-t))J]\boldsymbol{w}(t), \quad s \in (t, t+\Delta t). \end{aligned} \tag{2.27}$$

From the expression (2.25) we obtain

$$(1-u(s)^2)^{1/2} = \frac{(1-u(t)^2)^{1/2}}{\cosh(cgH(t)(s-t)) + u(t)\sinh(cgH(t)(s-t))}, \tag{2.28}$$

so

$$\boldsymbol{v}(s) = \frac{\cos(cH(t)(s-t))I + \sin(cH(t)(s-t))J}{\cosh(cgH(t)(s-t)) + u(t)\sinh(cgH(t)(s-t))}\boldsymbol{v}(t), \quad s \in (t, t+\Delta t). \tag{2.29}$$

These results motivate the choice of the integration scheme for Eq. (2.12),

$$\begin{aligned} \boldsymbol{m}_{n+1} &= \frac{(\boldsymbol{m}_n \cdot \boldsymbol{h}_n)\cosh(cgH_n\Delta t) + \sinh(cgH_n\Delta t)}{\cosh(cgH_n\Delta t) + (\boldsymbol{m}_n \cdot \boldsymbol{h}_n)\sinh(cgH_n\Delta t)}\boldsymbol{h}_n \\ &\quad + \frac{\cos(cH_n\Delta t)I + \sin(cH_n\Delta t)J}{\cosh(cgH_n\Delta t) + (\boldsymbol{m}_n \cdot \boldsymbol{h}_n)\sinh(cgH_n\Delta t)}\boldsymbol{h}_n \times (\boldsymbol{m}_n \times \boldsymbol{h}_n), \end{aligned} \tag{2.30}$$

where $\boldsymbol{m}_{n+1} = \boldsymbol{m}(t_{n+1})$, $\boldsymbol{m}_n = \boldsymbol{m}(t_n)$, $\boldsymbol{h}_n = \boldsymbol{h}(t_n)$, $H_n = H(t_n)$, and $\Delta t = t_{n+1} - t_n$.

The algorithm (2.30) is unconditionally stable for all values of Δt. Of course, the quality of the approximation suffers as Δt increases. However, the algorithm explicitly displays the relationship between the size of Δt and the local error in the time integration.

The rate of precession of $\boldsymbol{m}$ around the polar axis is governed by H, the magnitude of the local effective field: in one time step, $\boldsymbol{m}$ precesses through an angle $H\Delta t$. Therefore, by properly choosing Δt, we can resolve the fastest precessional motion in a given number of time steps per period. Since H varies over the course of a simulation, we have a natural and direct means to adjust the size of Δt to the current dynamical state, while maintaining the resolution of the precessional motion.

Other algorithms for the numerical integration of the LLG equation have been proposed recently by Nigam [14] and E and Wang [15].

2.3 Computing Equilibrium Configurations

The analysis in the preceding section suggests the following algorithm for finding the equilibrium spin configuration in a bilayer. Starting from a given equilibrium state $\boldsymbol{M} = \{\boldsymbol{M}_i : i \in I\}$ at time t_0, one uses Eq. (2.6) to compute the magnetic field $\boldsymbol{H}_i$ in each layer at t_0. Having found $\boldsymbol{H}_i(t_0)$ for all $i \in I$, one advances in time to $t_1 = t_0 + \Delta t$ and uses Eqs. (2.2) and (2.30) to compute $\boldsymbol{M}$ at t_1. If Δt is sufficiently small, $\boldsymbol{M}(t_1)$ is a close approximation of the state of the system at time t_1. One continues this process, finding approximations of the state of the system at successive times $t_n = t_0 + n\Delta t$, $n = 1, 2, \ldots$, until equilibrium is reached.

3 Numerical Results

The algorithm of the preceding section has been used to study hysteresis phenomena in hard/soft bilayers that are driven by an applied field $\boldsymbol{H}_a$ that is uniform, constant in time, and parallel to the planes of the atomic layers. The expression for the effective magnetic field, Eq. (2.6), decomposes into an in-plane component,

$$\begin{aligned}\boldsymbol{H}_i \times \boldsymbol{e}_z = \boldsymbol{H}_a \times \boldsymbol{e}_z \;+\; & \frac{1}{M_i}\left[J_{i,i+1}(\boldsymbol{m}_{i+1} - \boldsymbol{m}_i) - J_{i,i-1}(\boldsymbol{m}_i - \boldsymbol{m}_{i-1})\right] \times \boldsymbol{e}_z \\ & - 2\frac{K_i}{M_i}(\boldsymbol{m}_i \cdot \boldsymbol{e}_y)\boldsymbol{e}_x, \quad i \in I, \end{aligned} \tag{3.1}$$

and an out-of-plane component,

$$\begin{aligned}\boldsymbol{H}_i \cdot \boldsymbol{e}_z \;=\; & \frac{1}{M_i}\left[J_{i,i+1}(\boldsymbol{m}_{i+1} - \boldsymbol{m}_i) - J_{i,i-1}(\boldsymbol{m}_i - \boldsymbol{m}_{i-1})\right] \cdot \boldsymbol{e}_z \\ & - 2\frac{K_i}{M_i}\boldsymbol{m}_i \cdot \boldsymbol{e}_z - 4\pi M_i \boldsymbol{m}_i \cdot \boldsymbol{e}_z, \quad i \in I. \end{aligned} \tag{3.2}$$

When the system is in an equilibrium state, the effective magnetic field is parallel (or antiparallel) to the magnetic spin; see Section 2.2. Hence, each $\boldsymbol{H}_i$ is a multiple of $\boldsymbol{m}_i$, and

Eq. (3.2) reduces to a homogeneous system of linear algebraic equations for the set of scalars $\{\boldsymbol{m}_i \cdot \boldsymbol{e}_z : i \in I\}$. In general, this system admits only the trivial solution, so the magnetic moments lie in the plane of the atomic layers. In the notation of Eq. (2.3), $\phi_i = 0$ for all $i \in I$ at equilibrium, and the only relevant variables are the in-plane angles $\{\theta_i : i \in I\}$. (Of course, the magnetic spin may have an out-of-plane component during the transient phase of the computation.)

In the numerical simulations we focus on the in-plane angle of the magnetic spin at equilibrium and investigate its behavior as a function of the strength H_a and the direction θ_a of the applied field,

$$\boldsymbol{H}_a = H_a \boldsymbol{h}_a, \quad \boldsymbol{h}_a = (\cos\theta_a, \sin\theta_a, 0)^{\mathrm{t}}. \tag{3.3}$$

The following computations refer to a bilayer configuration consisting of $N_h = 115$ atomic layers of Sm-Co (a hard material) and $N_s = 100$ atomic layers of Fe (a soft material). A different configuration is used in Section 3.3, where we make a comparison with some magneto-optical measurements. Table 1 gives the values of the material parameters A, K, and M, as well as the values of the coupling coefficient J ($J = Ad^{-2}$, $d = 2$ Å). The gyromagnetic constant is $\gamma = 1.1052 \cdot 10^8/(2\pi)$ $\mathrm{sec}^{-1}\mathrm{oersted}^{-1}$. In all cases, the damping coefficient $g = 0.5$.

Table 1: Numerical values of the parameters.

	A (erg/cm)	J (erg/cm^3)	K (erg/cm^3)	M (emu/cm^3)
Fe	$2.8 \cdot 10^{-6}$	$7.0 \cdot 10^9$	$1.0 \cdot 10^3$	1,700
Interface	$1.8 \cdot 10^{-6}$	$4.5 \cdot 10^9$	–	–
Sm-Co	$1.2 \cdot 10^{-6}$	$3.0 \cdot 10^9$	$5.0 \cdot 10^7$	550

3.1 Rotational Hysteresis

The case $H_a = 4800$ oersteds is typical, at least for moderate values of H_a (see Section 3.2).

In a first set of simulations, we computed the equilibrium state as a function of the angle θ_a, first increasing θ_a from 0 to 2π, then decreasing θ_a from 2π to 0. At each value of θ_a, we started the computation from the equilibrium state for the preceding value of θ_a.

The simulations show that the equilibrium spin configurations for increasing θ_a ($0 < \theta_a < 2\pi$) and decreasing θ_a ($2\pi > \theta_a > 0$) are mirror images of each other. Figure 1 shows two sets of magnetic spin configurations at equilibrium for various values of θ_a, one set (left) as θ_a increases from 0 to 2π, the other set (right) as θ_a decreases from 2π to 0. The heavy dots represent the endpoints of the magnetic spin (a unit vector) in each layer for various angles θ_a; the values of θ_a, in degrees, are indicated near the top layer. (The dots merge into a solid line where the magnetic spins in adjacent layers are close.)

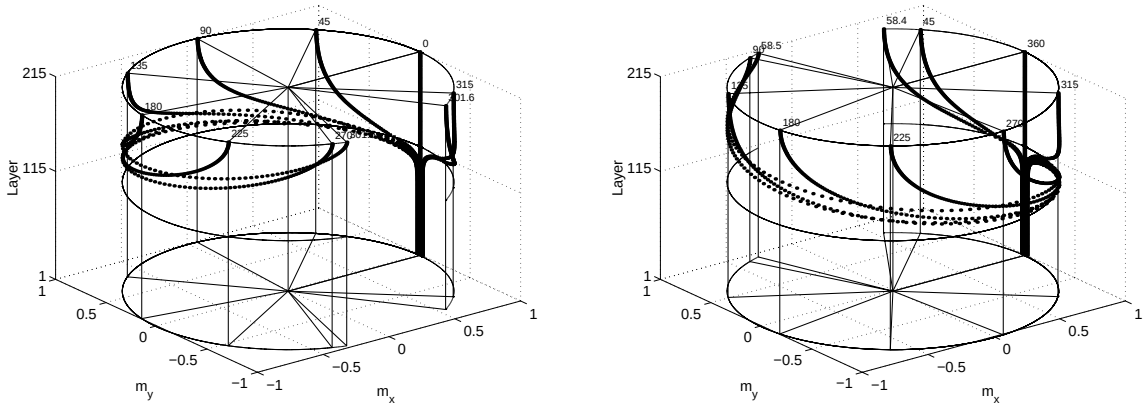

Figure 1: Equilibrium spin configurations; $H_a = 4800$ oersteds. Left: θ_a increasing. Right: θ_a decreasing.

Notice that the chirality ("handedness") of the chain of magnetic spins changes suddenly from positive at $\theta_a = 301.5$ to negative at $\theta_a = 301.6$ degrees and from negative at $\theta_a = 58.5$ to positive at $\theta_a = 58.4$ degrees. Figure 2 zooms in on this phenomenon. It shows the chain of spins at $\theta_a = 301.5$ and $\theta_a = 301.6$ degrees from a different viewpoint.

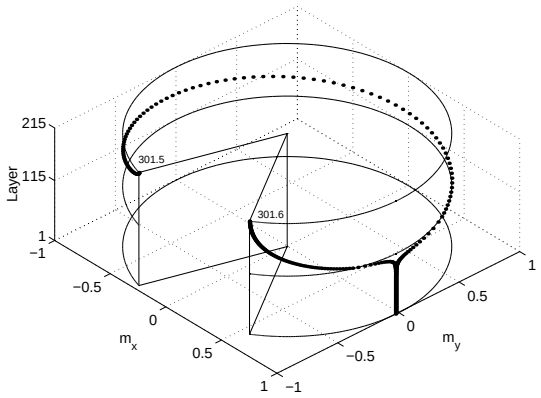

Figure 2: Equilibrium spin configuration; $H_a = 4800$ oersteds.

Figure 3 shows the change of chirality in a different way. Here, we have plotted the in-plane angle θ_i against the layer index i for increasing values of θ_a. (The graphs for decreasing values of θ_a are obtained by symmetry.)

Notice that, in all cases, the spin is fixed along the easy axis ($\theta_i = 0$) in most of the hard layers; it begins to deviate from the easy axis only as one approaches the interface ($i = 115$). The first derivative is discontinuous at the interface, and the tangent is vertical in the top layer ($i = 215$). First, the graph changes continuously (but not monotonically)

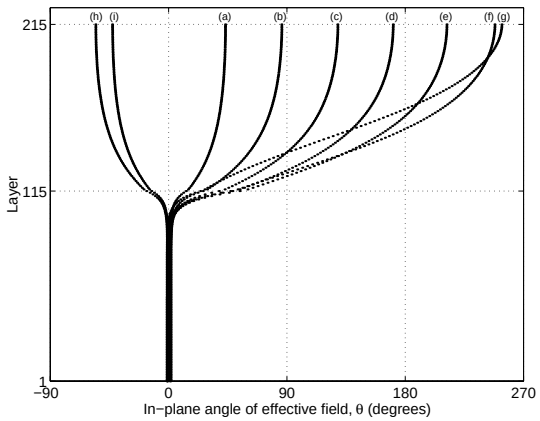

Figure 3: In-plane angle θ_i vs. i; $H_a = 4800$ oersteds; (a) $\theta_a = 45$, (b) $\theta_a = 90$, (c) $\theta_a = 135$, (d) $\theta_a = 180$, (e) $\theta_a = 225$, (f) $\theta_a = 270$, (g) $\theta_a = 301.5$, (h) $\theta_a = 301.6$, (i) $\theta_a = 315$ degrees.

as θ_a increases from 0 to 301.5 degrees, while maintaining its right handedness (θ_i increases with i). Then it changes discontinously at $\theta_a = 301.6$ degrees: it becomes left handed (θ_i decreases with i). Finally, it changes continuously again as θ_a increases further, maintaining its left handedness, to return to the original graph ($\theta_i = 0$ for all $i \in I$) as θ_a reaches 360 degrees.

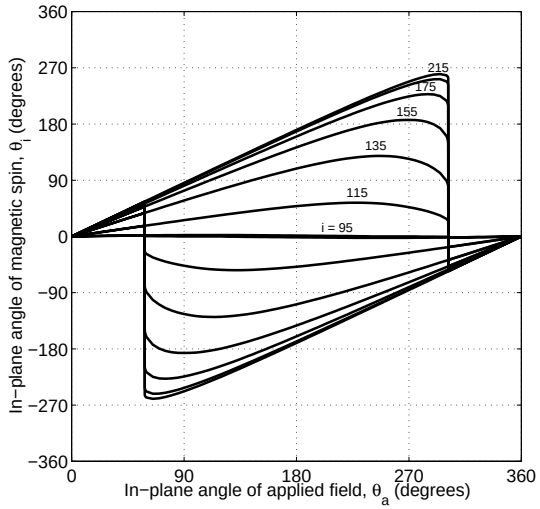

Figure 4: In-plane angle θ_i vs. θ_a; $H_a = 4800$ oersteds; $i = 95, 115, 135, 155, 175, 195, 215$.

The change in chirality is irreversible and induces *rotational hysteresis* in the chain of magnetic spins. The in-plane angle of each spin vector traverses a different trajectory as the applied field rotates 360 degrees in the forward and backward direction. The hysteresis loop has the same shape, and particularly the same width, in all layers. Its vertical dimension

contracts gradually as one descends through the soft layers, to disappear entirely in the hard layers somewhat below the interface; see Fig. 4.

3.2 Two Types of Rotational Hysteresis

We now vary the strength of the applied field, H_a. We recall (Fig. 4) that, as θ_a increases from 0, the chirality changes discontinuously from positive to negative as the direction of the applied field deviates sufficiently from the easy axis. We denote the critical value of the angle θ_a by θ_c ($\theta_c = 301.5\ldots$ at $H_a = 4800$ oersteds.) Figure 5 shows the variation of θ_c with H_a.

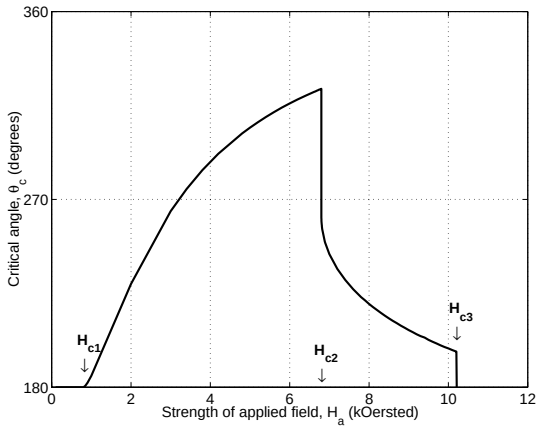

Figure 5: Variation of θ_c with H_a.

We discuss the different types of behavior in detail. (The remarks in parentheses give numerical values obtained for the standard configuration.)

3.2.1 $\mathbf{0 < H_a < H_{c1}}$

The magnetization process is reversible as long as H_a is sufficiently small, $0 < H_a < H_{c1}$ ($H_{c1} \approx 800$ oersteds). Figure 6 shows the in-plane angle of the magnetic spin in the top layer, θ_N, vs. θ_a; θ_N oscillates, the graph for increasing values of θ_a coincides with the graph for decreasing values of θ_a, and only the direction in which the graph is traversed is reversed. The behavior of θ_i in other layers is similar.

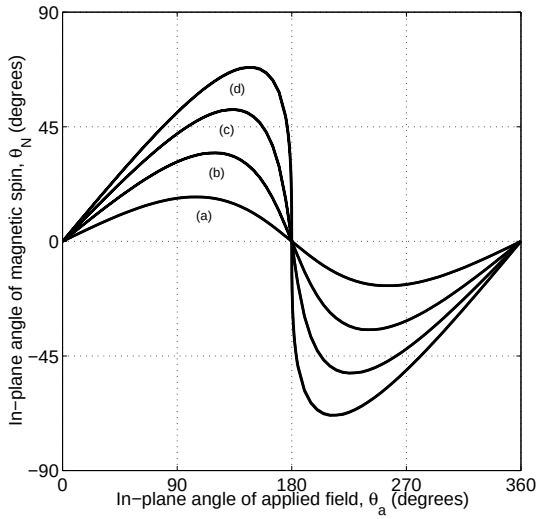

Figure 6: No hysteresis below H_{c1}. In-plane angle θ_N (top layer) vs. θ_a, (a) $H_a = 200$, (b) $H_a = 400$, (c) $H_a = 600$, (d) $H_a = 800$ oersteds.

3.2.2 $\mathbf{H_{c1} \leq H_a < H_{c2}}$

The first critical value of H_a, H_{c1}, is reached when the slope of the graph of θ_N (and of θ_i for all i) vs. θ_a in Fig. 6 becomes vertical. The graph of θ_c vs. H_a (Fig. 5) is continuous and has a zero slope at $H_a = H_{c1}$. From here on, the magnetization process is irreversible. The spins show *rotational hysteresis* of the type discussed in the preceding section, with a basic period of 2π. The graph of θ_i vs. θ_a for increasing values of θ_a separates from the graph for decreasing values of θ_a. The separation is symmetric around $\theta_a = \pi$.

The width of the hysteresis loop increases monotonically from 0 at $H_a = H_{c1}$ to some value less than 2π (≈ 286 degrees) at the next critical value, $H_a = H_{c2}$. Figure 7 shows the in-plane angle in the top layer as a function of θ_a, for various values of H_a. (The vertical scale differs from Fig. 6.)

3.2.3 $\mathbf{H_{c2} \leq H_a < H_{c3}}$

At $H_a = H_{c2}$ ($H_{c2} \approx 6798$ oersteds), the angle θ_c shows a pronounced discontinuity (θ_c drops from 323.1 degrees at $H_a = 6798$ oersteds to 259.9 degrees at $H_a = 6799$ oersteds) and the hysteresis loop suddenly narrows. Beyond H_{c2}, it continues to narrow, but it does not collapse entirely. At the next critical value, $H_a = H_{c3}$, θ_c is still greater than π ($\theta_c \approx 197.0$ degrees); see Fig. 8.

The cause of the discontinuity at $H_a = H_{c2}$ can be seen in Fig. 9, where we have

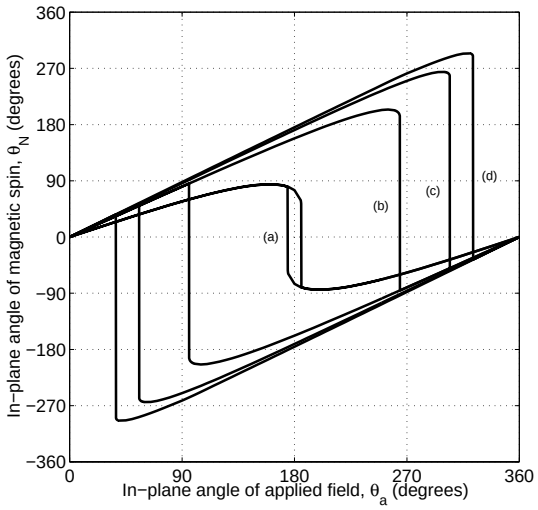

Figure 7: Rotational hysteresis in (H_{c1}, H_{c2}). In-plane angle θ_N (top layer) vs. θ_a, (a) $H_a = 1000$, (b) $H_a = 3000$, (c) $H_a = 5000$, (d) $H_a = 6797$ oersteds.

plotted θ_i against i; cf. Fig. 3. (The bottom 80 layers of hard material, where θ does not deviate noticeably from 0, are not included in this figure.) At H_{c2}, the chain of spins has been stretched to its widest extent; it can no longer support the (almost 280-degree) span in the top layer, stiffens suddenly, and becomes more like a rigid rod. The rod-like behavior is apparent from the increasing range where the chain is almost vertical. The stiffening of the chain of magnetic spins continues as H_a increases to H_{c3}.

The structural change in the chain of spins has some of the characteristics of a phase transition. For example, we observe a significant increase in the equilibration time (by two orders of magnitude) as θ_a approaches θ_c; see Fig. 10. Also, the increasing size of the rigid domain near H_{c2} is reminiscent of a diverging correlation length.

3.2.4 $\mathbf{H_a \geq H_{c3}}$

At $H_a = H_{c3}$ (H_{c3} between 10,200 and 10,300 oersteds), the magnetic spin configuration begins to show an entirely new behavior. So far, the spins have always maintained a fixed orientation in the hard layers: along the easy axis (apart from small deviations near the interface) and in the *positive* x direction. As the applied field rotated, the orientation of the magnetic spins changed only in the soft layers (and in a few hard layers just below the interface). The result was a change of the chirality of the chain of magnetic spins, which led to rotational hysteresis with a basic period 2π. At $H_a = H_{c3}$, the field energy becomes sufficiently large for the first time to change the orientation of the spin in the *hard* layers to the *negative* x direction and thus move the chain of magnetic spins over its entire length.

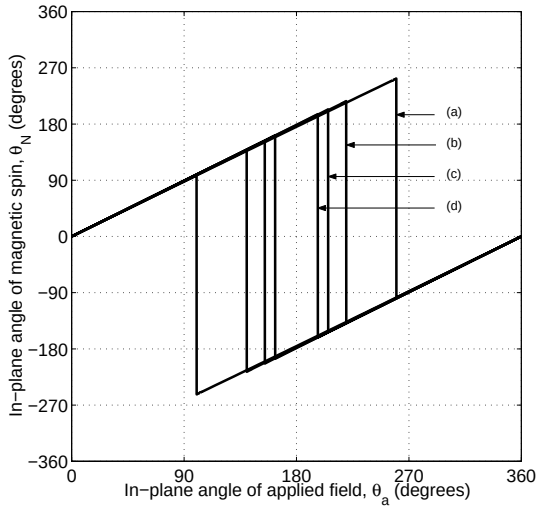

Figure 8: Rotational hysteresis in (H_{c2}, H_{c3}). In-plane angle θ_N (top layer) vs. θ_a, (a) $H_a = 6799$, (b) $H_a = 8000$, (c) $H_a = 9200$, (d) $H_a = 10,200$ oersteds.

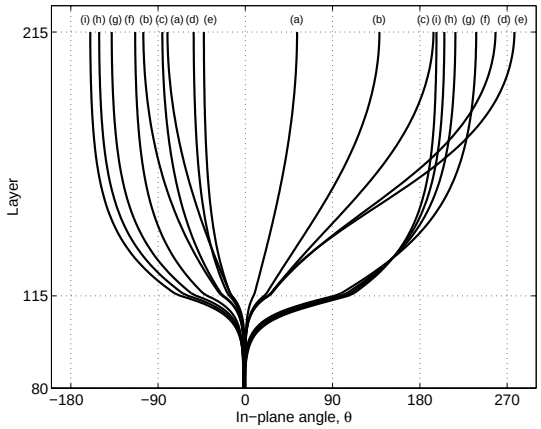

Figure 9: In-plane angle θ_i vs. i; (a) $H_a = 1000$, (b) $H_a = 2000$, (c) $H_a = 3000$, (d) $H_a = 5000$, (e) $H_a = 6000$, (f) $H_a = 7000$, (g) $H_a = 8000$, (h) $H_a = 9000$, (i) $H_a = 10,000$ oersteds. Right branches: θ_a just below θ_c, left branches: θ_a just above θ_c.

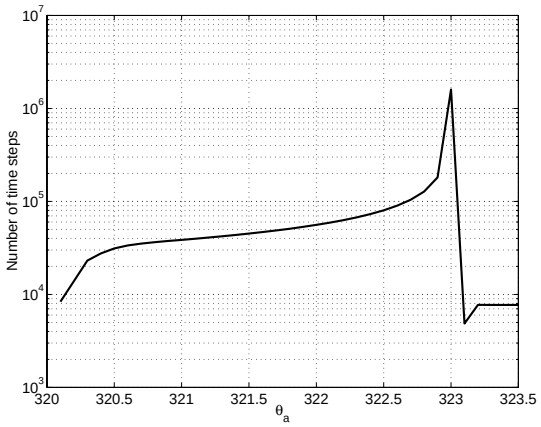

Figure 10: Equilibration time near θ_c; $H_a = 6797$ oersteds, $\theta_c = 323.0$ degrees.

The reason for the existence of a critical value H_{c3} is apparent from Fig. 9. As H_a increases from H_{c2} to H_{c3}, the graph of θ_i vs. i steepens in the upper layers, while it gets stretched more and more in the lower soft layers and the upper hard layers. (Notice the pivot point, a little below the 130th layer.) At H_{c3}, the tension in the upper hard layers can no longer be supported, and the spin chain relaxes by shifting in its entirety by 180 degrees in the hard layers.

The magnetization reversal develops as follows. As θ_a first increases from 0, the magnetic spin in the hard layers is fixed in the positive x direction; θ_i increases continuously from 0 as one goes up through the soft layers to match θ_a, the direction of the applied field, in the top layer. When θ_a passes a critical value θ_c say, a little beyond π, the spins in the hard layers flip to the negative x direction, to remain there until θ_a reaches the value $\theta_c + \pi$. The exact value of θ_c depends on H_a and decreases to π as H_a increases beyond H_{c3}. The spin again rotates continuously with a positive chirality as one goes up through the soft layers, to match θ_a in the top layer.

This scenario is repeated every time the difference $\theta_a - \theta_c$ passes a multiple of π. As a result, the chain of spins maintains a positive chirality, and each θ_i keeps increasing with θ_a. The jump of θ_i, which is a full 180 degrees in (most of) the hard layers, diminishes as one goes up through the layers, to vanish eventually in the top layer, where θ_N changes continuously with θ_a; see Fig. 11 (left).

When the direction of the applied field is reversed, the magnetic spin first retraces its steps, maintaining its positive chirality, until $\theta_a - \theta_c$ passes the first multiple of π. At that point, the chirality changes from positive to negative, to remain negative from there on. The same scenario as when θ_a increases (a flip of the spins in the hard layers every time $\theta_a - \theta_c$ passes a multiple of π) is repeated, but now in the opposite direction; see Fig. 11 (right). As a result, θ keeps decreasing with θ_a until it is back to 0.

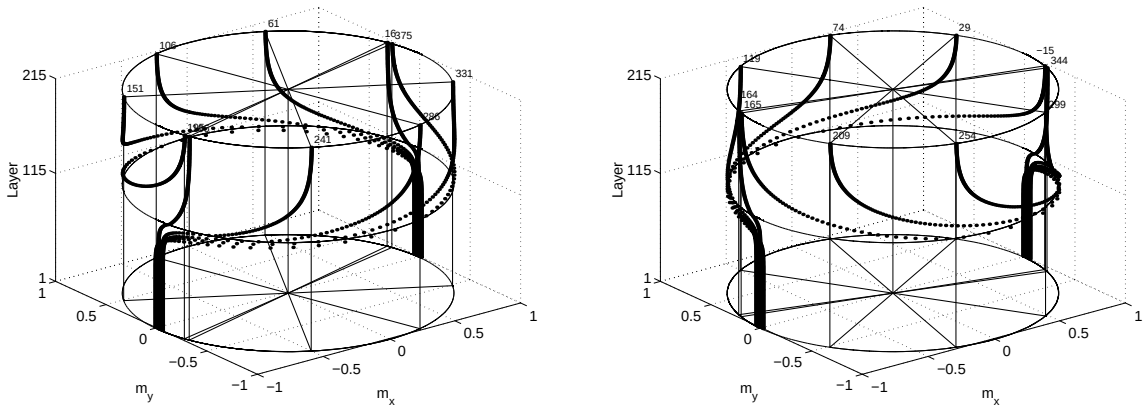

Figure 11: Equilibrium spin configurations; $H_a = 10,400$ oersteds. Left: θ_a increasing, right: θ_a decreasing.

The preservation of chirality during a full-circle rotation of the applied field is illustrated in Figs. 12 and 13.

Figure 12 gives θ_i vs. i for increasing values of θ_a. (The graphs for decreasing values of θ_a are obtained by symmetry.) The value $H_a = 10,400$ oersteds is just above H_{c3}. This figure should be compared with Fig. 3 for the standard case, $H_a = 4800$ oersteds.

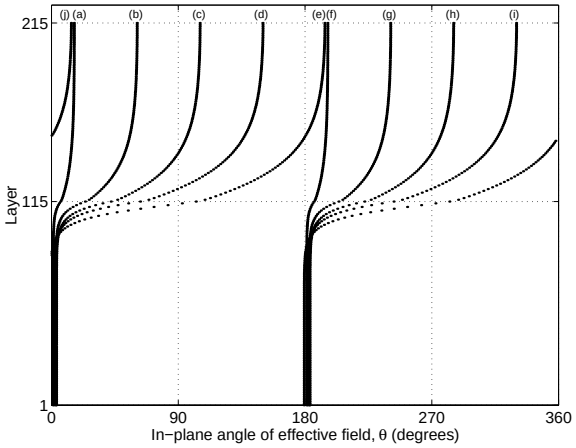

Figure 12: In-plane angle θ_i vs. i; $H_a = 10,400$ oersteds; (a) $\theta_a = 16$, (b) $\theta_a = 61$, (c) $\theta_a = 106$, (d) $\theta_a = 151$, (e) $\theta_a = 195$, (f) $\theta_a = 196$, (g) $\theta_a = 241$, (h) $\theta_a = 286$, (i) $\theta_a = 331$, (j) $\theta_a = 375$ degrees.

Figure 13 shows three graphs: one graph (c) is along the diagonal; the other two (a and b) are symmetric with respect to the diagonal. The outer graph (a) shows the variation of the in-plane angle of the magnetic spin, θ_i, with θ_a for $i = 85$ (hard layer). The part

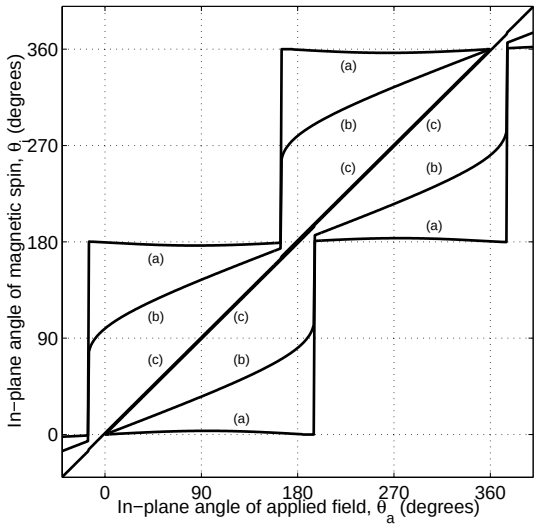

Figure 13: In-plane angle θ_i vs. θ_a; $H_a = 10,400$ oersteds; (a) $i = 85$ (hard layer), (b) $i = 115$ (interface), (c) $i = 215$ (top layer).

below the diagonal is traversed in the upward direction as θ_a increases from 0; the part above the diagonal is traversed in the downward direction as θ_a decreases from 360 degrees. The spin is oriented in either the positive or the negative x direction. The first transition going up occurs at $\theta_c \approx 196$ degrees, the first transition coming down occurs at $2\pi - \theta_c$, and subsequent transitions occur at every multiple of π beyond θ_c. The center graph (c) shows θ_i for $i = 215$ (top layer). The orientation of this spin varies continuously with θ_a and is perfectly reversible. Finally, the middle graph (b) shows θ_i for $i = 115$ (at the interface). Here, the spin rotates continuously until it jumps. The jumps occur at θ_c $(2\pi - \theta_c)$ and at every multiple of π beyond θ_c. The graphs for the remaining layers fill the space between the ones drawn in the figure. The main point to observe is that the graphs for θ_a increasing always increase and stay below the diagonal, while those for θ_a decreasing always decrease and stay above the diagonal. Hence, chirality is preserved in both cases.

When the direction of θ_a is reversed, θ_i crosses the diagonal as soon as $\theta_a - \theta_c$ is a multiple of π; after crossing, it remains on the part of the graph situated on the newly reached side of the diagonal. Because there is a gap between the graphs for θ_i in the interior layers and the diagonal, the orientation of the magnetic spin shows rotational hysteresis in all layers (except the top one). But this hysteresis is caused by a full-length transition of the chain of magnetic spins, rather than the partial-range transition that was responsible for the hysteresis below H_{c3}.

As H_a increases beyond H_{c3}, the jumps in Fig. 13 move closer to the nearest multiple of π, but the general pattern persists.

3.3 Comparison with Experiment

Quantities such as the magnetic moment are fundamental to describe the state of the system, but they are not directly measurable in an experiment. Measurable quantities are the *magnetization angle* (or *apparent angle*), α, and the *torque density*, T. The magnetization angle is associated with the vector sum of the in-plane components of the magnetic moments,

$$\alpha = \tan^{-1} \frac{\sum_{i \in I} M_{i,y}}{\sum_{i \in I} M_{i,x}} = \tan^{-1} \frac{\sum_{i \in I} M_i \sin \theta_i}{\sum_{i \in I} M_i \cos \theta_i}. \tag{3.4}$$

The torque density T (erg/cm^2) is defined by the expression

$$T = H_a d \sum_{i \in I} M_i \sin(\theta_a - \theta_i); \tag{3.5}$$

it is the normal component of the vector $\boldsymbol{T}$,

$$\boldsymbol{T} = d \sum_{i \in I} (\boldsymbol{M}_i \times \boldsymbol{H}_a) = H_a d \sum_{i \in I} M_i (\boldsymbol{m}_i \times \boldsymbol{h}_a). \tag{3.6}$$

In Fig. 14, we compare results for the magnetization angle with experimental data. The data were obtained by magneto-optical means for a bilayer consisting of $N_h = 100$ atomic layers of Sm-Co and $N_s = 250$ atomic layers of Fe; the simulation curves also refer to this configuration [11]. The measurements were done at relatively low fields ($H_a = 360, 600,$ and 840 oersteds) and for a limited range of directions ($\theta_a = 0 : 10 : 230$ degrees).

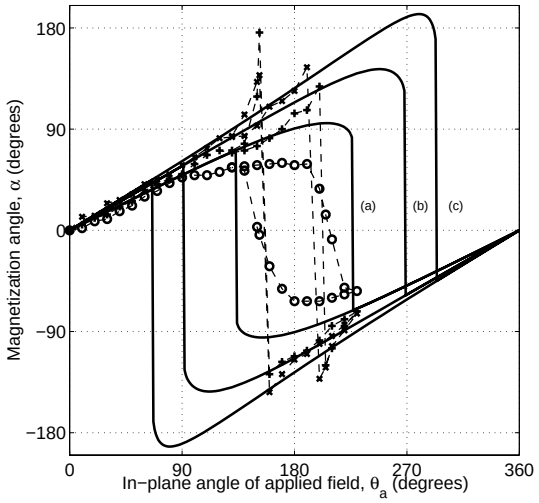

Figure 14: Magnetization angle; (a) $H_a = 360$ (**o**), (b) $H_a = 600$ (+), and (c) $H_a = 840$ ($\times$) oersteds.

There is certainly qualitative agreement, but the simulations generally yield wider hysteresis loops than the experiments. In fact, the discrepancy becomes greater as the field strength increases. This behavior can be explained by the fact that the model used in the simulations is a single-domain model, which does not allow for the important phenomenon of nucleation and motion of nanodomains. As a result, the demagnetization energy is seriously overestimated. In realistic simulations, one must use multidimensional models and allow for lateral inhomogeneities [11].

For completeness, we also give the computational results for the magnetization angle and torque density for the standard configuration considered in the preceding sections; see Figs. 15 and 16.

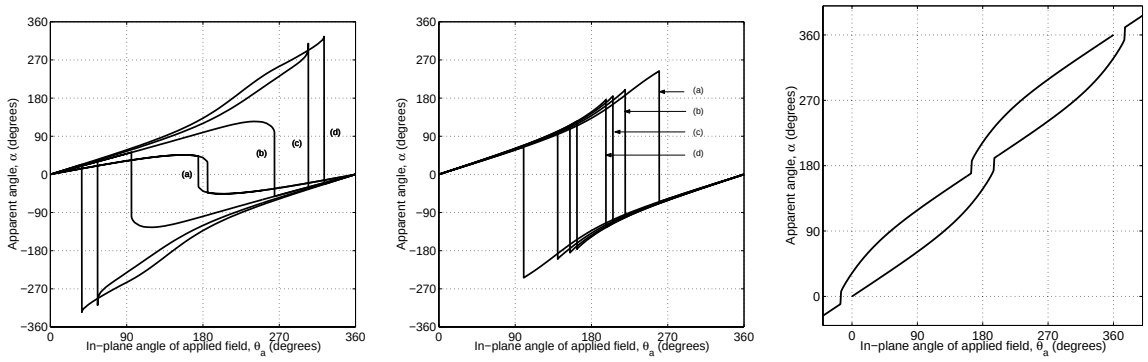

Figure 15: Hysteresis loops of the magnetization angle. Left: (a) $H_a = 1000$, (b) $H_a = 3000$, (c) $H_a = 5000$, (d) $H_a = 6797$ oersteds. Center: (a) $H_a = 6799$, (b) $H_a = 8000$, (c) $H_a = 9200$, (d) $H_a = 10,200$ oersteds. Right: $H_a = 10,400$ oersteds.

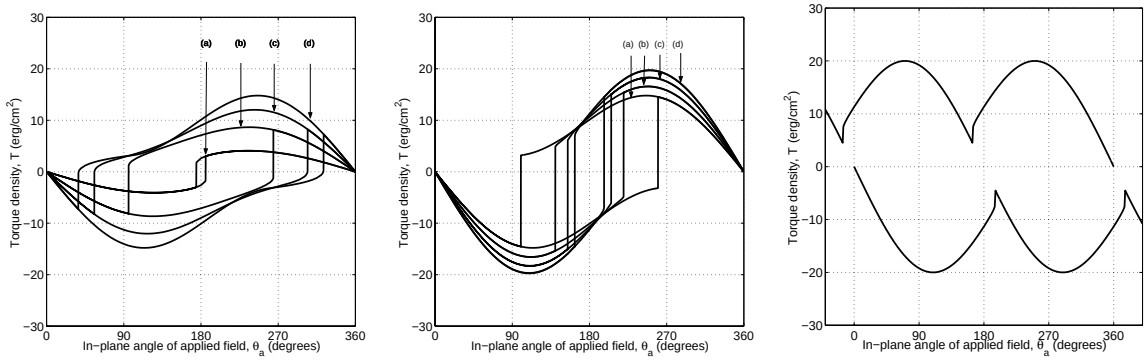

Figure 16: Hysteresis loops of the torque density. Left: (a) $H_a = 1000$, (b) $H_a = 3000$, (c) $H_a = 5000$, (d) $H_a = 6797$ oersteds. Center: (a) $H_a = 6799$, (b) $H_a = 8000$, (c) $H_a = 9200$, (d) $H_a = 10,200$ oersteds. Right: $H_a = 10,400$ oersteds.

Both the magnetization angle and the torque density reflect the behavior of the mag-

netic moments. Their hysteresis loops expand between H_{c1} and H_{c2}, show a discontinuity at $H_a = H_{c2}$, contract between H_{c2} and H_{c3}, and show period doubling beyond H_{c3}.

Notice that the graph of the apparent angle appears to develop cusps near the discontinuities when H_a is below H_{c2} (Fig. 15, left, curve (c)). In fact, at $H_a = 4800$ oersteds (not shown), the value of α exceeds the value of θ_a at the last data point ($\alpha = 306.9$ at $\theta_a = 301.5$ degrees). The origin of this anomaly is to be found in the definition of the apparent angle. Once the spins in the soft layers rotate beyond 180 degrees, their contribution to the vector sum in Eq. (3.4) changes sign. As a result, the magnetization angle may overtake θ_a.

Experimental torque measurements at comparable values of H_a show similarly shaped graphs, with extrema at approximately the same values of θ_a, but significantly narrower hysteresis loops [10].

3.4 Energy Density

It is interesting to see how the energy density of the equilibrium spin configuration depends on θ_a and how this dependence varies with H_a.

Figure 17 summarizes the results of the simulations, again for the standard configuration considered in the preceding sections. (The vertical scales vary from one subfigure to the next.) The graph is smooth as H_a increases from 0. It develops a cusp at $\theta_a = \pi$ as H_a approaches H_{c1} (Fig. 17, top left). The cusp develops into a discontinuity, which shifts to increasing values of θ_a and becomes more pronounced as H_a increases beyond H_{c1} to H_{c2} (Fig. 17, top right). The discontinuity shifts back and diminishes as H_a increases beyond H_{c2}, until it disappears entirely when H_a reaches the value H_{c3} (Fig. 17, bottom left). At $H_a = H_{c3}$, a new equilibrium state with a significantly lower energy density, namely the state where the spin in both the hard and the soft layers is flipped by 180 degrees, becomes accessible, and the energy density curve becomes smooth on the two halves of the interval, with a peak exactly at $\theta_a = \pi$ (Fig. 17, bottom right).

A contour plot of the energy surface is given in Fig. 18. One recognizes the outline of the curve of critical values θ_c of Fig. 5.

3.5 Determination of H_{c3}

The exact determination of H_{c3} is delicate. If H_a is already above H_{c3}, but the increment in θ_a is taken too large, the configuration of the magnetic spins may show the same qualitative behavior as when H_a is below H_{c3}. The spin in the hard layers stays fixed in the positive x direction, there is a critical value θ_c of θ_a where the chirality of the chain of spins changes

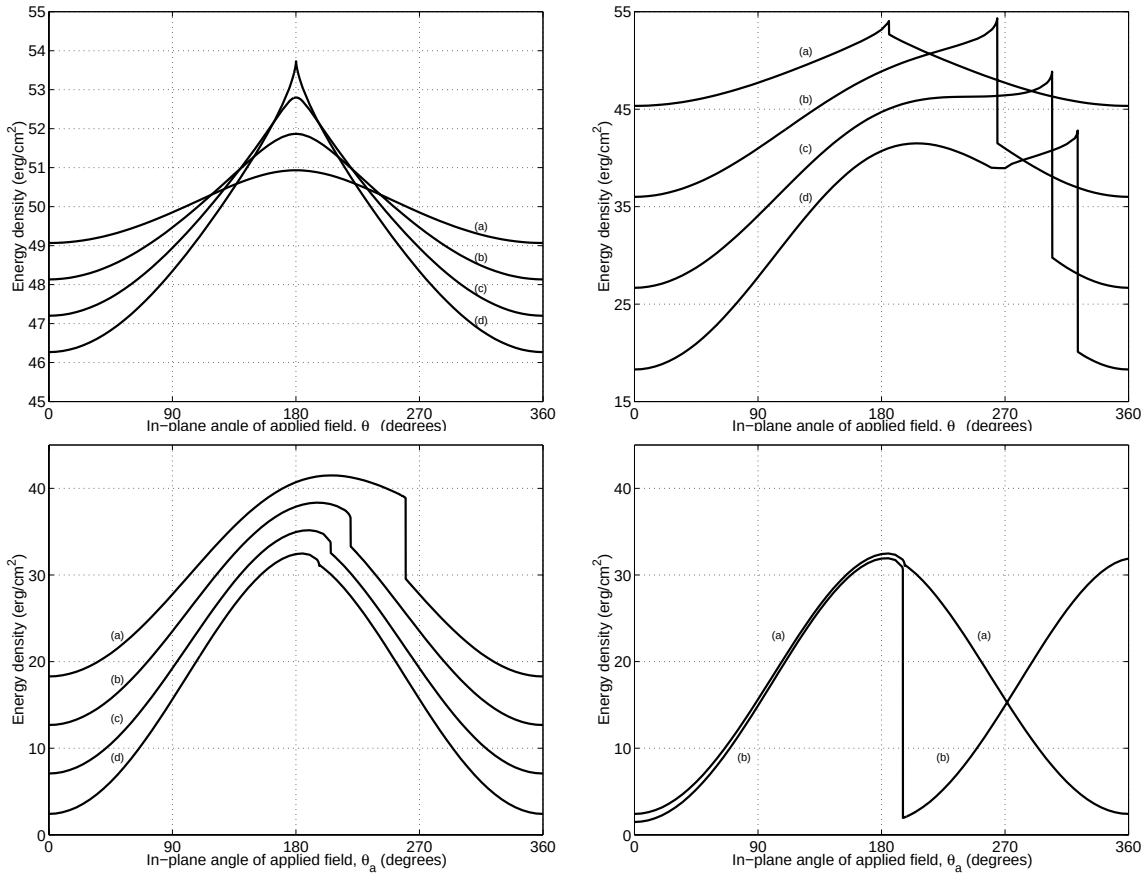

Figure 17: Total energy density at equilibrium. Top left: (a) $H_a = 200$, (b) $H_a = 400$, (c) $H_a = 600$, (d) $H_a = 800$ oersteds. Top right: (a) $H_a = 1000$, (b) $H_a = 3000$, (c) $H_a = 5000$, (d) $H_a = 6797$ oersteds. Bottom left: (a) $H_a = 6799$, (b) $H_a = 8000$, (c) $H_a = 9200$, (d) $H_a = 10,200$ oersteds. Bottom right: (a) $H_a = 10,200$, (b) $H_a = 10,400$ oersteds.

from positive to negative, and the system continues to show hysteretic behavior. The qualitative change in the configuration of the magnetic spins at $H_a = H_{c3}$ described above and illustrated in Fig. 11 becomes apparent only if the increment in θ_a is sufficiently small, and even more so as H_a gets closer to H_{c3}. Figure 19 shows some hysteresis loops for θ_N, α, and T, which were obtained for three values H_a, each greater than H_{c3}, with 5-, 10-, and 20-degree increments of θ_a, respectively. (The increasing increment explains the increasing slope of the hysteresis loops.) The total equilibrium energy density of these states (not shown) follows the pattern of the curve (a) in Fig. 17, bottom right.

In the neighborhood of H_{c3}, the rotational hysteresis phenomenon is apparently rate dependent: it is possible to reach different states by choosing different increments of θ_a. Table 2 illustrates this point. Here, $H_a = 10,400$ oersteds, which is just above the critical

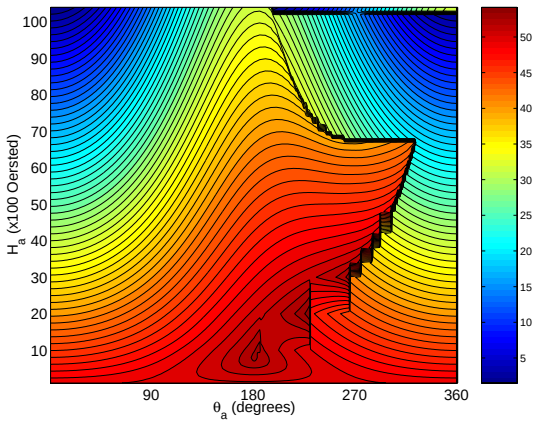

Figure 18: Contour plot of the total equilibrium energy density as a function of H_a (vertical axis) and θ_a (horizontal axis).

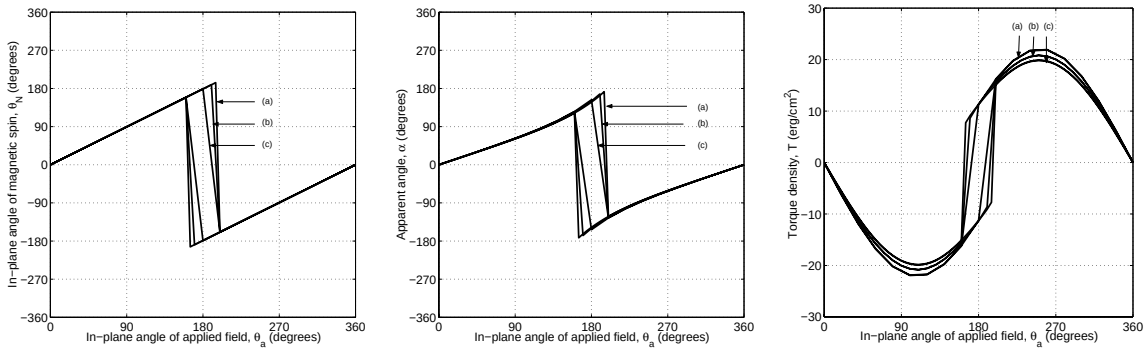

Figure 19: "Rotational hysteresis" above H_{c3}; (a) $H_a = 10,300$, (b) $H_a = 11,000$, (c) $H_a = 11,900$ oersteds. Left: in-plane angle θ_N (top layer); center: magnetization angle α; right: torque density T.

value H_{c3}. We determined with a 0.1 degree increment that the spin in the hard layers changes direction when θ_a is between 195.5 and 195.6 degrees; the energy drops from 60.048 to 2.159 erg/cm^2. The same state is reached when the increment is 1 degree and θ_a is increased from 195 to 196 degrees. But when the increment is 5 degrees and θ_a is increased from 195 to 200 degrees, we continue to see rotational hysteresis, and the energy drops only a fraction to 49.397 erg/cm^2.

Table 2: Total equilibrium energy density E (erg/cm^2); $H_a = 10,400$ oersteds; increments $\Delta\theta_a = 0.5, 1,$ and 5 degrees.

θ_a	190.0	194.0	194.5	195.0	195.5	196.0	196.5	197.0	197.5	198.0	200.0
E	58.707	59.701	59.819	59.935	60.048	2.194	2.238	2.284	2.312	2.381	2.590
E	58.708	59.701	–	59.935	–	2.194	–	2.285		2.381	2.590
E	58.711	–	–	59.935	–	–	–	–	–	–	49.397

4 Conclusions

In this report we have addressed the important issue of magnetization reversal in layered spring magnets. We have used a one-dimensional model of a film consisting of atomic layers of a soft material on top of atomic layers of a hard material, with strong coupling at the interface, assuming no variation in the lateral directions. The state of such a system is described by a chain of magnetic spin vectors. Each spin vector behaves like a spinning top driven by the local magnetic field and subject to damping. The dynamics are described by a system of LLG equations, Eq. (2.5), coupled with a variational equation for the magnetic field, Eq. (2.6). The numerical algorithm for the integration of the LLG equations, Eq. (2.30), preserves the magnitude of the magnetization vector at all times.

The results of numerical simulations show that a layered spring magnet exhibits rotational hysteresis with a basic period of 360 degrees at moderately strong fields and rotational hysteresis with a basic period of 180 degrees at strong fields. The former type of hysteresis is induced by a partial-length transition of the chain of magnetic spins; the transition occurs only in the soft material and causes a change of chirality. The hysteresis in strong fields is induced by a full-length transition of the chain of spins in both the hard and the soft layers; it is much weaker than the rotational hysteresis at moderately weak fields and can cover any period that is a multiple of the base period.

The numerical results for the torque and magnetization angle agree qualitatively with the experimental data but differ at the quantitative level. In particular, the one-dimensional model seriously overestimates the demagnetization energy, since it does not allow for the nucleation and motion of nanodomains. In realistic simulations, lateral inhomogeneities must be taken into account.

Acknowledgments

Most of the numerical simulations were carried out by Jaime Hernandez Jr. (University of Texas at El Paso), who was a participant in the Energy Research Undergraduate Laboratory Fellowship program at Argonne National Laboratory (summer 2000).

References

[1] E. F. Kneller and R. Hawig, "The exchange-spring magnet: A new material principle for permanent magnets," IEEE Trans. Mag., **27** (1991), 3588–3600.

[2] J. M. D. Coey and R. Skomski, "New magnets from interstitial intermetallics," Physica Scripta, **T49** (1993), 315–321.

[3] R. Skomski and J. M. D. Coey, "Giant energy product in nanostructured two-phase magnets," Phys. Rev. B, **48** (1993), 15812–15816.

[4] R. Fischer, T. Leinewebber, and H. Kronmüller, "Fundamental magnetization processes in nanoscaled composite permanent magnets," Phys. Rev. B, **57** (1998), 10723–10732.

[5] E. E. Fullerton, J. S. Jiang, C. H. Sowers, J. E. Pearson, and S. D. Bader, "Structure and magnetic properties of exchange-spring Sm-CO/Co superlattices," Appl. Phys. Lett., **72** (1998), 380–382.

[6] J. S. Jiang, E. E. Fullerton, C. H. Sowers, A. Inomata, S. D. Bader, A. J. Shapiro, R. D. Shull, V. S. Gornakov, and V. I. Nikitenko, "Spring magnet films," IEEE Trans. Magn., **35** (2000), 3229.

[7] L. Landau and E. Lifshitz, "On the theory of magnetic permeability in ferromagnetic bodies," Physik. Z. Soviet Union, **8** (1935), 153–169.

[8] T. L. Gilbert, "A Lagrangian formulation of gyromagnetic equation of the magnetization field," Phys. Rev., **100** (1955), 1243.

[9] J. Fidler and T. Schrefl, "Micromagnetic modeling—the current state of the art," J. Phys. D: Appl. Phys., **33** (2000), R135–R156.

[10] S. David, S. S. P. Parkin, E. E. Fullerton, C. Platt, A. Berkowitz, J. S. Jiang, and S. D.Bader, "Field dependent reversal modes in exchange-spring thin films from rotational hysteresis analysis," J. Appl. Phys. (to appear).

[11] R. D. Shull, A. J. Shapiro, V. S. Gornakov, V. I. Nikitenko, J. S. Jiang, H. G. Kaper, G. K. Leaf, and S. D. Bader, "Spin spring behavior in exchange coupled soft and high-coercivity hard ferromagnets," J. Appl. Phys. (to appear).

[12] J. S. Jiang, H. G. Kaper, and G. K. Leaf, "Hysteresis in layered spring magnets," Preprint ANL/MCS-P867-0101; Discrete and Dynamical Systems—Series B, **1** (2001), to appear.

[13] H. N. Bertram, "Theory of magnetic recording," Cambridge University Press, 1994.

[14] N. Nigam, "Efficient micromagnetic calculations," Third SIAM Conf. on Mathematical Aspects of Materials Science, Philadelphia, Pennsylvania; May 2000.

[15] Weinan E and X. P. Wang, "Numerical methods for the Landau–Lifshitz equation," SIAM J. Numer. Anal. (to appear).